The Importance of Schottky Barrier Height in Plasmonically Enhanced Hot-Electron Devices

Shenyou Zhao, Yanting Yin, Jun Peng, Yiliang Wu, Gunther G. Andersson, Fiona J. Beck*

S. Zhao, Dr. J. Peng, Dr. Y. Wu, Dr. F. J. Beck
Research School of Electrical, Energy and Materials Engineering
Australian National University
Acton, ACT 2601, Australia
E-mail: fiona.beck@anu.edu.au

Dr. Y. Yin, Prof. G. G. Andersson
Flinders Institute for Nanoscale Science and Technology
Flinders University
Adelaide SA 5042, Australia
Flinders Microscopy and Microanalysis
College of Science and Engineering
Flinders University
Adelaide, SA 5042, Australia

Abstract

Plasmonically enhanced hot-electron (PEH) photodiodes are a new class of optoelectronic device with the potential to be selective to spectral position, polarization, and bandwidth. Reported solid-state PEH devices based on metal nanoparticles have generally have low performance, in part due to low collection efficiency of photogenerated hot electrons. We find a correlation between the measured external quantum efficiency (EQE) and the temperature at which the ALD TiO_2 is deposited by atomic layer deposition in Au-TiO_2 based PEH photodiodes. By investigating the material properties of the TiO_2 we demonstrate that the change in EQE is driven by a change in the Schottky barrier height. Our results show that lowering the Schottky barrier height increases the collection efficiency of hot electrons over the junction, in agreement with existing analytical models. This work demonstrates the crucial role that the interface plays in hot electron devices in general, and indicates that this is an important design consideration for the improvement of PEH photodetectors.

1. Introduction

Plasmonically enhanced hot-electron (PEH) photodiodes are a new class of optoelectronic device based on the collection of hot electrons generated by the decay of plasmonic resonances. The excitation of localized surface plasmons results in strong, tunable absorption in metal nanostructures, caused by collective oscillation of conduction electrons in the metal driven by incident electromagnetic radiation.[1] The spectral position, polarization, and bandwidth of the localized surface plasmon resonances can be tuned by tailoring the composition, size, and shape of the metal nanostructures,[2,3] offering the possibility for highly selective PEH-based optoelectronic devices.[4,5] These types of devices have the potential to be employed in photodetection applications that require sensitivity at wavelengths that are not easily targeted by cost-effective semiconductor materials, for example UV an IR detection [Gong, Sobhani].

The performance of a PEH device is determined by three main processes: light absorption, hot-carrier generation, and hot-carrier transport and collection. Plasmons are excited, then decay and transfer energy to hot electrons. The hot electrons will dissipate energy as heat due to carrier relaxation.[1] However, by forming a Schottky junction between the metal nanostructure and a semiconductor, hot electrons with sufficient energy can be injected over the barrier and collected before their energy is lost.[1]

Absorption in the nanostructure is the first factor determining the performance of the devices and has been studied by numerous works. The absorption cross section of metal nanoparticles at resonance can be much larger than the physical diameter of the metal nanoparticles ,[6] so very high absorption can be achieved. Both narrow band tunability [7] and broad band absorption [8] can be realised by changing the geometry of plasmonic nanostructures.

Only a fraction of the absorbed energy will result in high-energy, hot electrons. Theoretical studies have shown that the electron density of states limits the efficiency of hot electron generation.[9,10] However, it has been suggested that the generation efficiency can be modified by changing the size

and shape of the metal nanoparticles.[2,3] In particular, Reineck et al. showed experimentally that the efficiency of hot-electron generation can be affected by the size of the metal nanoparticles.[2] In addition, Zhang and colleague have demonstrated that the shapes of metal nanocrystals have significant effect on the plasmonic electrons.[3]

The transport and collection of the hot electrons from metal nanoparticles to the adjacent semiconductor is also of importance in determining the quantum efficiency. The transport and collection processes consist of ballistic and non-ballistic transport in the metal, hot-electron injection over the Schottky barrier, and conduction through the semiconductor. Ballistic transport is necessary for efficient collection of hot electrons, which is limited by mean free path of the energetic electrons in the metal nanoparticles.[11]

In addition, the Schottky barrier height (SBH) is an important factor affecting the efficiency of PEH injection over Schottky barrier at the metal-semiconductor interface as only electrons with sufficient energy to overcome the Schottky barrier will be injected into the conduction band of the semiconductor.[10,12] Once injected, the electron relaxes to the conduction band edge, and the Schottky barrier prevents the back injection into the metal, hence supressing recombination of the hot electron-hole pair and further dissipation of the electronic energy.

It is known that the characteristics of Schottky junctions are sensitively dependent on the metal-semiconductor interface.[13] In particular, the optoelectronic properties of oxide semiconductors are known to be sensitive to the deposition method and parameters (see for example ref [15]). Arshad and colleagues proposed a fabrication method of Au/TiO_2 nanorod arrays for photo-electrochemical measurement and determined the SBH of 0.23eV at the interface between Au and amorphous TiO_2 using X-ray photoelectron spectroscopy (XPS) analysis on valence band maximum.[14] They claimed that the low SBH that exists at the interface is beneficial to the effective charge separation of Au/TiO2. Despite this work, there is no detailed experimental evidence to show the relationship between the SBH and the collection efficiency of hot electrons through the interface.

In this work, we present a TiO$_2$ /gold nanoparticles (Au NPs) /nickel oxide (NiO) photodiode for photoelectric energy conversion via plasmonically enhanced hot electrons. The TiO$_2$ is a n-type semiconductor material that readily forms a Schottky junction with Au and been widely used in solar cells and photodetectors due to its optical and electronic properties and good chemical resistance.[15,16] The NiO is a p-type semiconductor with a large bandgap and acts as a hole-transporting material, preventing back-injection of electrons from the back contact.[17–19] We find that the processing temperature of the TiO$_2$ significantly impacts the performance of the device. The maximum external quantum efficiency (EQE) of the PEH devices at peak of the localized surface plasmon resonance decreases with increasing deposition temperature from 250°C to 400°C. By studying the surface morphology and material properties, as well as band alignment at the interface between Au and TiO$_2$ using photoelectron spectroscopy analysis, we show that this effect is due to a change in the Schottky barrier height. This finding provides experimental evidence to show that optimising barrier height is critical for collecting the hot electrons in PEH devices.

2. Results and Discussion

In this section, we experimentally investigate the optical, electrical and material properties of PEH devices with TiO$_2$ semiconductor layers fabricated at five different deposition temperatures. The characteristics of these devices were studied using optical transmittance and reflectance measurements, current-voltage characterisation, Scanning Electron Microscopy (SEM), X-ray Diffraction (XRD) analysis, X-ray Photoelectron Spectroscopy (XPS), UV-light Photoelectron Spectroscopy (UPS), and Inverse Photoelectron Spectroscopy (IPES).

2.1. Effect of Deposition Temperature on the Performance of PEH Devices and Analysis of Optical and Electrical Properties

Figure 1a) shows the architecture of the PEH devices under investigation, consisting of n-type TiO$_2$ deposited at various temperatures on a transparent front contact consisting of fluorine tin oxide

(FTO) coated glass. Gold nanoparticles (Au NPs) are deposited on top of the TiO_2 and result in a dense coverage, as shown in Figure 1b). A thin layer of p-type NiO is then deposited to block the back-transfer of electrons from the Au NP to the Au back contact, while allowing the efficient transfer of holes. Figure 1c) shows a schematic of the energy levels in the device. Light is incident from the FTO glass and partially absorbed by the Au NPs due to the excitation of localized surface plasmons. Hot electron-hole pairs can be then generated, and high energy electrons are injected over the Schottky barrier formed between the Au NPs and the TiO_2. Lastly, the electrons and holes are transferred through the TiO_2 (electrons) and NiO (holes) to be collected at their respective contacts.
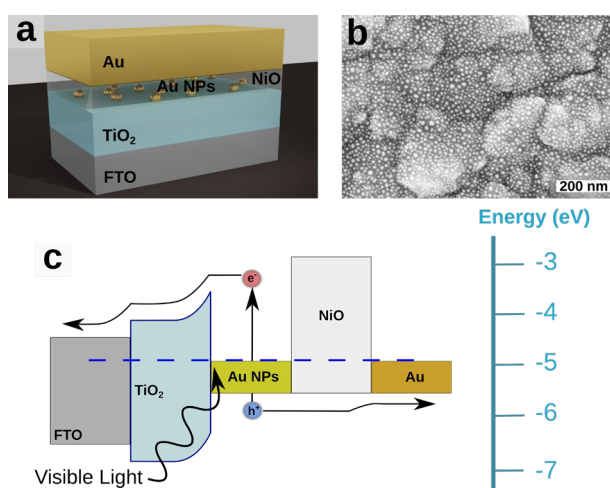

Figure 1. a). Schematic of a plasmonically enhanced hot-electron device, which consists of n-type TiO_2 deposited on FTO coated glass, Au NPs, p-type NiO, and gold electrode; b). SEM image of Au NPs deposited on TiO_2 coated FTO glass with scalebar of 200 nm; c). Schematic of the theoretical band alignment in the device, illustrating the Schottky junction formed between Au and TiO_2. Hot electrons with sufficient energy could be injected over the Schottky barrier height (SBH).

EQE is a measure of the performance of a device, and is calculated as the ratio of the number of electrons collected by the device to the number of incident photons.[20] Figure 2a) shows the absorption spectra for FTO/TiO_2/NiO samples with (red, solid line) and without (blue, dashed line) Au NPs. The sample with Au NPs has a clear absorption peak at a wavelength of 620 nm due to a

localized surface plasmon resonances in the Au NPs. Figure 2b) shows the EQE spectra for a typical plasmonically enhanced hot-electron (PEH) device with Au NPs (red, solid line) and a reference device without Au NPs (blue, dashed line). The TiO_2 in both devices were deposited at 250°C. It is clear that the PEH device has a significant enhancement in the EQE compared with the reference device, corresponding to the absorption due to localized surface plasmon resonances. The peak of the EQE spetra is above 1% at wavelength of 600 nm, which is consistent with previous measurements in the literature. [2] The slight shift between the peaks of the EQE and absorption spectra is attributed to the change in the refractive index and thickness of materials surrounding the Au NPs. The high absorption and high EQE values below wavelengths of 400 nm are due to the strong absorption of high energy photons by TiO_2 which has a bandgap corresponding to a wavelength of 360-400 nm in both the reference and the PEH Au NPs device. Conversely, the EQE peak at a wavelength of ~ 600 nm is only observed in the device with Au NPs, indicating that it is due to the plasmonically-enhanced generation of hot electrons in the device. [21,22]
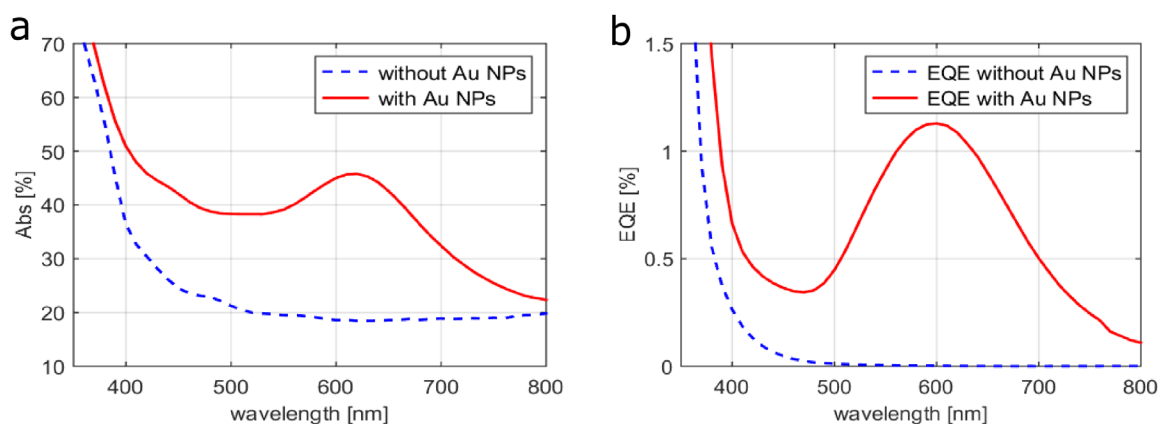

Figure 2. a). Absorption spectra of FTO/TiO₂/Au NPs/NiO with and without Au NPs; b). Representative EQE spectra of FTO/TiO₂/Au NPs/NiO/Au photodiodes with and without Au NPs. The blue dashed lines are reference samples without Au NPs and the red solid lines are samples with Au NPs. The TiO₂ in these specific devices was deposited at 250°C.

To investigate the effect of deposition temperature on the performance of PEH devices, we compare the performance of PEH devices with TiO_2 deposited at different temperatures via atomic layer

deposition (ALD). As described in detail in the experimental section below, the TiO_2 samples deposited at different temperatures experienced subsequent high temperature steps during the annealing of the Au NPs (270°C for 30 minutes) and the post-annealing of sputtered NiO (300°C for 60 minutes). Previous work has demonstrated that the crystal structure of ALD TiO_2 is formed during the deposition process and cannot be formed by post-annealing of ALD-grown amorphous TiO_2.[23] Therefore, we do not expect the annealing processes at relatively low temperatures (< 400°C) to affect the crystallinity and properties of the ALD TiO_2.

Figure 3 shows EQE measured at the localized surface plasmon resonance peak, for devices with TiO_2 deposited at five different temperatures. The 'EQE average' (blue squares with error bar) is calculated from at least four devices for each temperature, while the 'EQE champion' (red star) is the highest record value among these devices. From Figure 3, the EQE at resonance has a strong dependence on the TiO_2 deposition temperature. The EQE at resonance for devices with TiO_2 deposited at 200°C is significantly lower than the others, while the EQE at resonance is highest for TiO_2 deposited at 250°C and then decreases with increasing deposition temperature.
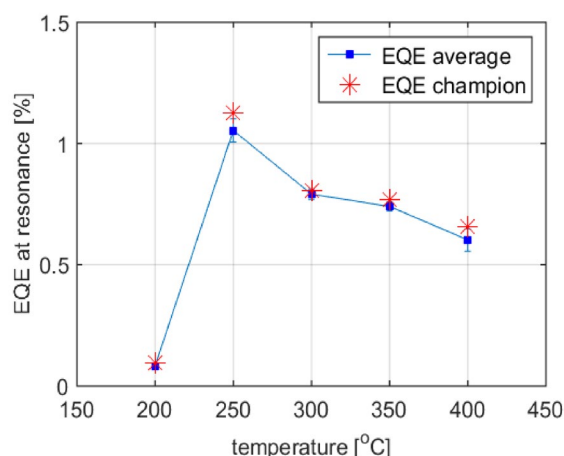

Figure 3. EQE at resonance (at a wavelength of 600±10 nm for all devices) as a function of ALD deposition temperature of TiO_2. The step of EQE measurements and thus the accuracy is 10 nm. The average EQE (blue squares) are calculated from measurement of 4-6 devices for

each temperature, while the red stars indicate the champion among the 4-6 devices. Error bars

show standard deviation for EQE measurements of individual PEH devices.

We will investigate the correlation between the EQE and the deposition temperature of atomic layer deposition (ALD) TiO_2 for temperatures above 250degC, in the following sections. It is known that the reaction temperature during ALD affects material properties such as crystallinity and electronic structures, including Fermi level, conduction band and valence band. [23–25] TiO_2 can form different phases such as amorphous, anatase, rutile, and brookie, which have different physical and chemical properties.[15,26] The crystallinity of TiO_2 was studied by Scanning Electron Microscopy (SEM) and X-ray Diffraction (XRD) analysis, and the results (shown in Figure S1 and S2 in the Supporting Information) demonstrate that the structure of ALD-grown TiO_2 changes from amorphous to anatase phase with increasing deposition temperature which is consistent with literature.[23–25] However, the exact temperature at which the TiO_2 formed by ALD begins to crystallise differs between studies.[23,25,27].

Next, the optical and electrical characteristics of the devices were investigated further. Absorption spectra of samples with various deposition temperatures are given in Figure S3 in the supporting information (SI). The results indicate that the absorption of the samples at the wavelength associated with the localized surface plasmon resonance is not significantly affected by the ALD deposition temperature. Current-Voltage measurements were also performed under both dark and light conditions and given in Figure S4 and S5 in the SI. The samples were illuminated with white light using a 550 nm optical longpass filter to avoid contributions to the short-circuit current density (J_{sc}) from absorption in the TiO_2. The photocurrent density is linearly dependent on the intensity of the incident light (as shown in Figure S6 in the SI). As expected, the trend of the J_{sc} agrees with that of the EQE and has an overall decrease with increasing deposition temperature from 250°C to 400°C, while the open-circuit voltage (V_{oc}) has an overall increase. In addition, the series resistance was extracted from the Current-Voltage measurements using the method presented by Cheung.[28,29]

Results show that 250-400°C samples have series resistance Rs = 35±5 Ω, but the amorphous TiO$_2$ deposited at 200°C has ~170 times higher resistance (as shown in Figure S7 in the SI).

The results from the above optical and electrical measurements indicate that the dependence of device performance on deposition temperature is not due to a change in absorption at the localized surface plasmon resonance, and hence hot electron generation efficiency, in the Au NPs. Instead, it is likely that the deposition temperature of the TiO$_2$ affects device performance by influencing the hot electron collection efficiency. While it is clear that the low conductivity of the TiO$_2$ deposited at 200°C will hinder the transport and collection of hot electrons, and hence significantly reduce the EQE, the correlation between EQE and deposition temperatures between 250-400°C requires further investigation, as presented in the following sections.

2.2. Analysis of Photoelectron Spectra and Determination of the SBH at the interface
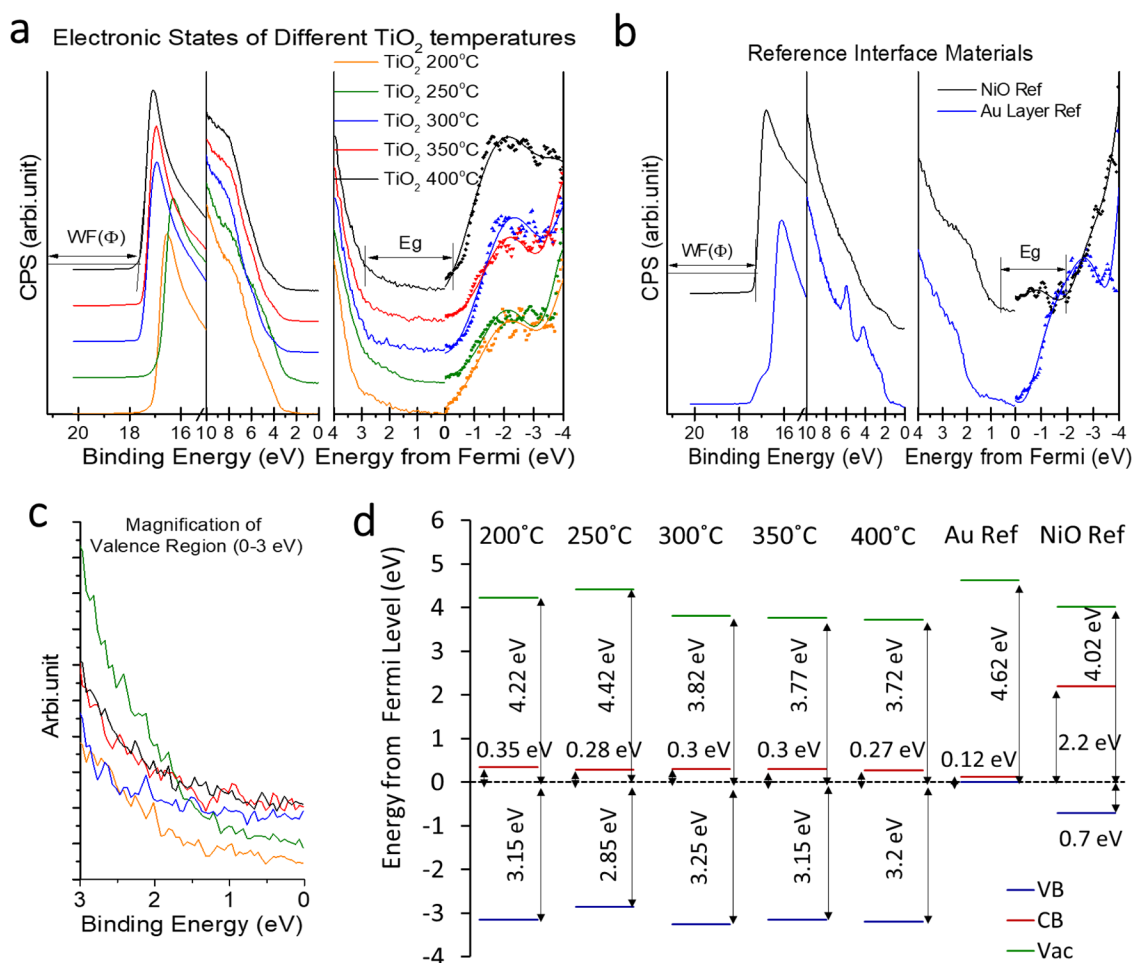
Figure 4. Energy level structure based on materials with Fermi alignment by UV-light Photoelectron Spectroscopy (UPS) measurements. a) UV-light Photoelectron Spectra and Inverse Photoelectron spectra of ALD TiO_2 fabricated with different temperatures. This plot shows the secondary electron cascades and valence/conduction electron distributions sequently from left to right; b) UV-light Photoelectron Spectra and Inverse Photoelectron spectra of reference high thickness Au layer and NiO substrate; c) The magnification of valence region shown in Figure 4 a) (0-3 eV). A range of electronic states along the valence electron distribution from 1.5 to 2.8 eV can be observed; d) Energy level plots of TiO_2 deposited at different temperatures, note that the Fermi level is aligned and shown as dash line. Data is also shown for pristine Au and pristine NiO.

Next, we investigate the energy bands in the materials in order to estimate the SBH formed between Au and TiO_2. By combining UV-light Photoelectron Spectroscopy (UPS) and Inverse Photoelectron Spectroscopy (IPES) measurements to investigate the electronic properties of TiO_2 and Au, the alignment of the energy bands at the interfaces between TiO_2 and Au can be derived.[14,30,31] Samples of ALD-deposited TiO2 at different temperatures, pristine Au and pristine NiO were all fabricated at a sufficient thickness (>30 nm) to cover the probing depth of the scope.

Figure 4 a) and b) shows the energy level structure of the samples as measured by UPS and IPES. Figure 4 a) shows the secondary electron cascades and valence/conduction electron distributions of TiO_2 deposited at different temperatures, and a gradual shift of secondary electron peak onset can be observed towards the higher binding energy region. Figure 4 b) delivers information about the electronic state distributions of Au and NiO as substrate reference.

The work function (WF), valence band maxima (VBM), and conduction band minima (CBM) can be extracted from the spectra in Figure 4 a) and b), as described in the experimental section, and are plotted in Figure 4 d). The work function was found to decrease with increasing ALD TiO_2 deposition temperature from 250˚C to 400˚C, while the conduction and valence band edges do not

show obvious changes in most of the TiO_2 samples, except for the 250˚C ALD TiO_2. In this case, the work function of the 250˚C TiO_2 increases to 4.42 ± 0.15 eV and the valence band maxima decreases to 2.85 ± 0.15 eV. In Figure 4 a), a range of electronic states along the valence electron distribution from 1.5 to 2.8 eV can also been observed and the magnification of such region is shown as green curve in Figure 4 c). This is an indication that such electronic states in the lower binding energy region of TiO_2 were produced due to this particular ALD processing temperature. These defect states can act as defect states below the valence band maxima,[32] decreasing the bandgap (Eg) significantly.

To determine the occurrence of Ti^{3+} defects states in TiO_2, in-situ X-ray photoelectron spectroscopy (XPS) was performed on the same samples. Details are given in the experimental section and the result is shown in Figure S8. It can be observed that the relative concentration of Ti^{3+} is highest for ALD-deposited TiO2 processed at 250˚C, indicating a higher presence of defect states.

For the Au reference sample, the work function was 4.62 ± 0.15 eV. A small band gap of 0.12 ± 0.15 eV was also observed due to the fact the Au was shortly exposed to air before test which may be slightly contaminated. The work function, valence band maxima and conduction band minima for NiO reference were respectively 4.02, 0.7 and 2.2 (± 0.15) eV due to its p-type characteristic.

The Fermi levels of individual components align at the interfaces of individual materials resulting in band bending.[33–36] The band bending at the interfaces could not be directly measured, as in reference,[33] because the height of the Au NPs is larger than 3 nm, meaning that the interface beneath the particles is out of the scope of UPS. Instead, the energy band bending at the interfaces can be estimated from the spectra in Figure 4, as reported in reference.[33,37,38] Arshad and colleagues calculated the SBH at the interface between TiO_2 and Au by XPS analysis on the valence band maxima,[14] however, Marri and Ossicini emphasized that the conduction band minima should be used determined that the SBH at the metal/n-type semiconductor interfaces.[31] Here we

calculate the SBH as the difference between the electron affinities in the TiO_2 and the Au (i.e. the energy difference between the conduction band minima and the vacuum level).[14][31]
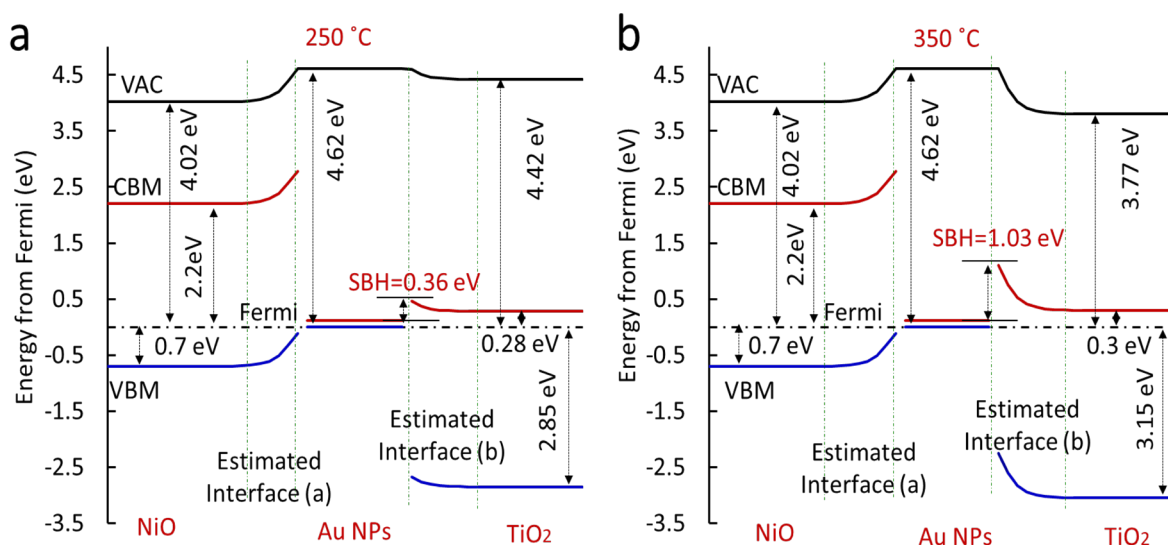

Figure 5 Energy level diagram based on measured a) NiO, Au and TiO_2 (250 ℃), estimated interface energy structures and Schottky barrier height (SBH); b) NiO, Au and TiO_2 (350 ℃), estimated interface energy structures and SBH. The energy level of the vacuum level (VAC), conduction band minima (CBM), and valence band maxima (VBM) are shown relative to the Fermi level, taken to be at 0eV.

The bandgap energies and SBH for the different samples are listed in the Table 1, and energy level diagrams, including estimated band structures at the interface, are plotted in Figure 5 for two different ALD TiO_2 process temperatures: 250℃ and 350℃. From Table 1 we can see that the SBH is different for all the samples under investigation. The SBH is significantly lower (0.36 eV) for 250℃ TiO_2 process temperature, and then increases sharply to 0.98 eV for 300℃. The SBHs then slightly increase with increasing process temperature from 300℃ to 400℃. The material bandgaps energies obtained from UV-Vis measurements (see Figure S9 in the SI) are also shown in Table 1 for comparison, and are consistent with that from UPS, providing a verification of the bandgap estimation.

It is important to note that the estimation of the SBH from the optical meanruements provided in Table one does not take into account the details of the Au-TiO₂ interface. As mentioned previously, Schottky junctions are sensitively dependent on the morphology of the interface as well as surface defect states. …[add discussion about electrical SBH measurement – briefly state that it is not always possible to measure and add references]

We also note that the work function of Au NPs can be affected by the size of Au NPs due to the charging of the NPs.[39] However, the size of the Au NPs is the same for all the samples (see Figure S10 in the SI), indicating that the change in SBH between samples is a function of deposition temperature of TiO_2, rather than changes in the morphology of the Au NPs.

Table 1. Band gap and SBH energies for various process temperatures of TiO_2.

TiO₂	200°C	250°C	300°C	350°C	400°C
Bandgap by UPS [eV]	3.50 ± 0.15	3.13 ± 0.15	3.55 ± 0.15	3.45 ± 0.15	3.47 ± 0.15
Bandgap by UV-vis [eV]	3.49 ± 0.2	3.26 ± 0.2	3.47 ± 0.2	3.46 ± 0.2	3.50 ± 0.2
SBH [eV]	0.63 ± 0.15	0.36 ± 0.15	0.98 ± 0.15	1.03 ± 0.15	1.05 ± 0.15

2.3. Understanding the Dependence of Performance of the PEH Devices on the SBH

To compare the experimentally determined dependence of performance of the PEH devices on the SBH, we calculate the hot-electron generation rate in Au nanoparticles, following the method of Govorov and colleagues. [9,12,40] These works provide analytical expressions to calculate the hot electron generation rate due to excitation and decay of plasmonic resonances in nanospheres of Au embedded in a dielectric medium. Within this framework, the total absorption is the sum of a classic absorption component and a semi-quantum component due to the generation of hot electrons:

$$Q_{tot} = Q_{hot} + Q_{abs} \tag{1}$$

Only a fraction of the generated hot electrons will have enough energy to be injected over the Schottky barrier, and absorbed energy that generates 'over-barrier' hot electron generation is defined as, Q_{ob}. We can then define a calculated quantum yield (QY) as

$$QY = \frac{Q_{ob}}{Q_{tot}}$$
(2)

The QY can be compared directly with the internal quantum efficiency (IQE, i.e. the fraction of absorption photons that are collected and generate current in a device) for an experimental device. A full description of the calculation is given in the SI (section S10).
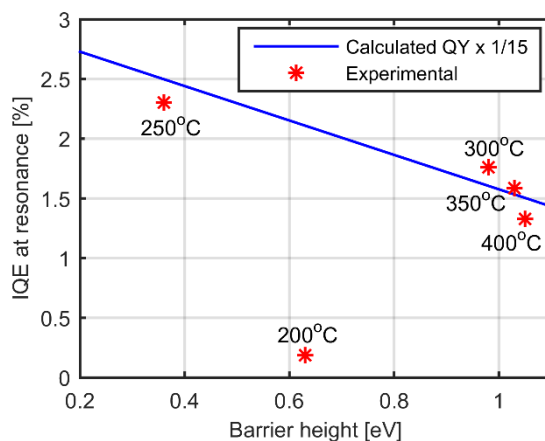

Figure 6 Internal quantum efficiency (IQE) at resonance determined from experimental measurements as a function of barrier height (red stars). Calculated quantum yield for 10 nm diameter spherical Au nanoparticles embedded in TiO₂ (blue line) shown for comparison.

Figure 6 shows the experimentally determined IQE at the plasmonic resonance as a function of Schottky barrier height (red stars), calculated by dividing the peak EQE (given in Figure 3) by the peak absorption (given in SI Figure S3). The calculated quantum yield is shown on the same graph for comparison, reduced by a factor of 15. The experimental data shows a clear linear trend between IQE at resonance of the PEH devices and SBH between Au and TiO₂, indicating that IQE of the PEH devices decreases with increasing SBH. The IQE at resonance for the devices with 200°C TiO₂ is not consistent with this trend as the overall performance of the device is reduced by the very high

resistivity of the TiO_2, as discussed above. The calculated results are much larger than the experimental results and represent an optimistic upper limit of what is achievable. However, the trend of measured IQE at resonance is well reproduced by the calculations of quantum yield, verifying that it is the change in the Schottky barrier height that is determining the performance differences between the measured PEH devices.

3. Conclusion

In this work, we experimentally demonstrate that varying the Schottky barrier height strongly affects the collection efficiency of hot electrons over the junction and hence the internal quantum efficiency of PEH devices. In doing so, we show that the material properties of the semiconductor play an important role in device performance, not only in determining the Schottky barrier heigth but also the conductivity. Using a range of optoelectronic characterisation and material characterisation we find that the effect of the deposition temperatures of TiO_2 on the EQE/IQE can be attributed to the change in the band energy of TiO_2, which in turn results in the change in SBH. .

These results demonstrate the crucial role that the interface plays in PEH devices and indicate that this is an important design consideration for the improvement of the performance of PEH devices.

4. Experimental Section

Sample Preparation: For each PEH photodiode test sample, a TiO_2 layer with thickness of ~75 nm was deposited on the precleaned fluorine tin oxide (FTO) substrate via atomic layer deposition (ALD). A thermal ALD system was used for depositing TiO_2 films using $TiCl_4$ precursors and H_2O, with N_2 as the purge gas. The reactor temperature was varied from 200°C to 400°C depending on the sample, and the carrier gas flows for $TiCl_4$ and H_2O were kept constant and set to 150 and 125 sccm, respectively. Each ALD cycle consisted of a 0.1s pulse of $TiCl_4$ followed by a 0.1s pulse of H_2O. Between each precursor pulse, the chamber was purged for 4.0s under a constant flow (300 sccm) of N_2. The thickness of TiO_2 by atomic layer deposition is slightly dependent on the

deposition temperature of the TiO_2. Due to the different deposition rates from 0.4 to 0.6 Å $cycle^{-1}$ at different temperatures, spectroscopic ellipsometry was used to measure the actual thicknesses of TiO_2 layer.

Next, an ultra-thin gold layer (nominal thickness of ~2.5nm) was deposited on the TiO_2 via thermal evaporation with the rate of 0.2 Ås^{-1}. The sample was then annealed at 270°C in N_2 atmosphere for 30 minutes before being cooled to 200°C at rate of 5°C per minute. The samples were then left to cool down to room temperature in air. The resulting Au nanoparticle films were imaged using a FEI Verios Scanning Electron Microscope (SEM) and particle diameters were measured using a custom-built MATLAB image recognition script. SEM images and corresponding nanoparticle diameters are shown in Figure S10 in the supporting information (SI). The average diameter of the Au NPs is 10±4 nm and is similar for samples with TiO_2 layers deposited at different temperatures.

The NiO_x layer was deposited by magnetron sputtering of a (3 inch) NiO target, at 180 W RF power, and using pure O_2 as a reactive gas at a pressure of 2 mTorr. The samples were then annealed at 300°C in air for 60 minutes. The target-substrate distance was 30 cm, and the chamber pressure was 20 mTorr. The deposition rate was ~0.045 Ås^{-1} as determined by a thickness measurement using spectroscopic ellipsometry. After deposition, the samples were stored in a nitrogen atmosphere.

Lastly, a 100 nm layer of gold was deposited on top of the sample, via thermal evaporation with the rate of 0.5-1.0 Ås^{-1}.

The thicknesses of TiO_2 and NiO were optimized by maximising the EQE at resonance of the PEH devices (see Figure S11 in the SI). Although 25 nm TiO_2 layer could provide the best performance for tested devices, 75±5 nm thickness of TiO_2 was used in this work since it is difficult to form successfully a Schottky junction with thickness of TiO_2 as thin as 25 nm.

Reference photodiode samples with architecture of FTO/TiO$_2$/NiO/Au and FTO/TiO$_2$/Au were fabricated at the same time as the PEH devices and were identical apart from the absence of Au NPs.

Samples were fabricated for UPS and XRD measurements, consisting of TiO$_2$ layers with thickness of 50±5 nm deposited on precleaned FTO substrates. TiO$_2$ films were fabricated with identical ALD methods as above.

Optical Characterization: The optical transmittance and reflectance spectra measured using a PerkinElmer Lambda 1050 UV/Vis/NIR spectrophotometer with an integrating sphere attachment. The absorbance, A, of the samples was obtained from the transmittance, T, and reflectance, R, as A = 1 - R - T. The bandgap energy of the TiO$_2$ films can also be determined using the absorbance spectra.

Current-Voltage (IV) Characterization: IV characteristics were investigated using a B1500A semiconductor device analyser and a custom-built measurement jig to make contact to the samples. Photocurrent measurements were conducted using the same measurement set-up in conjunction with a custom-built optical setup which focused light to a spot with size slightly smaller than the active area of the devices (2x3 mm^2). The optical setup was equipped with a Xenon high pressure short arc lamp as the light source and a monochromator which transmits a narrow band wavelength of light from 350nm to 800nm. External quantum efficiency (EQE) response was measured using a calibrated silicon photodiode sensor. The EQE was calculated from the measured photocurrent and the incident illumination intensity, which was obtained from the responsivity and measured photocurrent of the silicon photodiode.

Ultraviolet Photoelectron Spectroscopy (UPS): UPS was applied to determine the occupied electron states of a sample surface and the minimum energy required for an electron to escape the surface (work function). [41,42] UV radiation with an excitation energy of 21.218 eV is directed onto the samples. The emitted electrons are detected with a Phoibos 100 electron energy analyser from SPECS. The work function of a sample was determined by extrapolating the cut-off of secondary

electron cascade[33,37] and valence band structure can be determined from the cut-off of high kinetic energy electron distribution of the acquired spectra.

Inverse Photoelectron Spectroscopy (IPES): IPES was used for determining the unoccupied electron states of the samples,[43,44] which based on electron in/photon out/ionised electron record mechanism. In IPES, a beam of electrons with specified energy is directed onto a sample surface, entering the unoccupied states and releasing photons with corresponding energy. The photons were detected by ionizing a mixed Ar/Actone gas inside a Geiger-Müller tube thus the intensity of electrons is recorded as a function of ionization. The electrons with specific kinetic energies comprise the IPE spectrum, which can be converted to photon energy, thus the electrons from the unoccupied states of a sample surface are known. By operating in situ-IPES subsequent to UPS, a complete energy band structure of the sample is acquired.

X-ray Photoelectron Spectroscopy (XPS): XPS was performed to investigate the elemental composition and the chemical states of the elements.[45] The instrument was operated by using Mg line radiation with a probing depth of around 10nm, which depends on the kinetic energy of the electrons emitted from a specific element. With the radiation of X-ray, the electrons are excited and emitted from the core level of atom. The XPS was done in the same ultra-high vacuum (UHV) chamber with UPS thus they were performed in-situ.

X-ray Diffraction (XRD) Analysis: XRD was performed with a PANalytical X'Pert Pro materials research diffractometer operated at a voltage of 45 kV and a current of 40 mA. Scans were performed at 2θ from 10° to 80°, with a step of 0.03° and scan speed of 2.3° min^{-1}.

Supporting Information
Supporting Information is available from the Wiley Online Library or from the author.

Fabrication Facility (ANFF). S. Zhao also acknowledges Dr. Kaushal Vora for assistance with ALD

TiO$_2$ fabrication and Dr. Zelio Fusco for valuable feedback and assistance with the schematic in

Figure 1.

Conflict of Interest

The authors declare no conflict of interest.

[1]   M. W. Knight, H. Sobhani, P. Nordlander, N. J. Halas, *Science (80-.).* **2011**, *332*, 702.
[2]   A. Sobhani, M. W. Knight, Y. Wang, B. Zheng, N. S. King, L. V. Brown, Z. Fang, P. Nordlander, N. J. Halas, *Nat. Commun.* **2013**, *4*, 1643.
[3]   B. Du, L. Lin, W. Liu, S. Zu, Y. Yu, Z. Li, Y. Kang, H. Peng, X. Zhu, Z. Fang, *Laser Photonics Rev.* **2017**, *11*, DOI: 10.1002/lpor.201600148.

References

[1]   V. Amendola, R. Pilot, M. Frasconi, O. M. Maragò, M. A. Iatì, *J. Phys. Condens. Matter* **2017**, *29*, 203002.

[2]   P. Reineck, D. Brick, P. Mulvaney, U. Bach, *J. Phys. Chem. Lett.* **2016**, *7*, 4137.

[3]   H. Zhang, A. O. Govorov, *J. Phys. Chem. C* **2014**, *118*, 7606.

[4]   C. Clavero, *Nat. Photonics* **2014**, *8*, 95.

[5]   M. L. Brongersma, *Proc. IEEE* **2016**, *104*, 2349.

[6]   H. Paul, C. F. Bohren, *Am. J. Phys.* **1983**, *51*, 327.

[7]   A. Sobhani, M. W. Knight, Y. Wang, B. Zheng, N. S. King, L. V. Brown, Z. Fang, P. Nordlander, N. J. Halas, *Nat. Commun.* **2013**, *4*, 1643.

[8]   W. Li, J. Valentine, *Nano Lett.* **2014**, *14*, 3510.

[9]   L. V. Besteiro, X. T. Kong, Z. Wang, G. Hartland, A. O. Govorov, *ACS Photonics* **2017**, *4*, 2759.

[10]   T. P. White, K. R. Catchpole, *Appl. Phys. Lett.* **2012**, *101*.

[11]   Y. K. Lee, H. Lee, C. Lee, E. Hwang, J. Y. Park, *J. Phys. Condens. Matter* **2016**, *28*, 254006.

[12]   A. O. Govorov, H. Zhang, Y. K. Gun'ko, *J. Phys. Chem. C* **2013**, *117*, 16616.

[13]   R. T. Tung, *Appl. Phys. Rev.* **2014**, *1*.

[14]   M. S. Arshad, Š. Trafela, K. Ž. Rožman, J. Kovač, P. Djinović, A. Pintar, *J. Mater. Chem. C* **2017**, *5*, 10509.

[15]   S. Dueñas, H. Castán, H. García, E. S. Andrés, M. Toledano-Luque, I. Mártil, G. González-Díaz, K. Kukli, T. Uustare, J. Aarik, *Semicond. Sci. Technol.* **2005**, *20*, 1044.

[16]   J. Peng, T. Duong, X. Zhou, H. Shen, Y. Wu, H. K. Mulmudi, Y. Wan, D. Zhong, J. Li, T. Tsuzuki, K. J. Weber, K. R. Catchpole, T. P. White, *Adv. Energy Mater.* **2016**.

[17]   L. Hu, J. Peng, W. Wang, Z. Xia, J. Yuan, J. Lu, X. Huang, W. Ma, H. Song, W. Chen, Y. B. Cheng, J. Tang, *ACS Photonics* **2014**, *1*, 547.

[18]   L. Xu, X. Chen, J. Jin, W. Liu, B. Dong, X. Bai, H. Song, P. Reiss, *Nano Energy* **2019**, *63*, 103860.

[19]   M. B. Islam, M. Yanagida, Y. Shirai, Y. Nabetani, K. Miyano, *ACS Omega* **2017**, *2*, 2291.

[20]   T. Markvart, L. Castañer, In *Solar Cells Materials, Manufacture and Operation (Second Edition)*; Elsevier, 2013; pp. 3–25.

[21]   Y. Tian, T. Tatsuma, *J. Am. Chem. Soc.* **2005**, *127*, 7632.

[22]   P. Reineck, G. P. Lee, D. Brick, M. Karg, P. Mulvaney, U. Bach, *Adv. Mater.* **2012**, *24*, 4750.

[23]   J. Aarik, A. Aidla, T. Uustare, V. Sammelselg, *J. Cryst. Growth* **1995**, *148*, 268.

[24]   J. Aarik, A. Aidla, A.-A. Kiisler, T. Uustare, V. Sammelselg, *Thin Solid Films* **1997**, *305*, 270.

[25]   W. Chiappim, G. E. Testoni, R. S. Moraes, R. S. Pessoa, J. C. Sag??s, F. D. Origo, L. Vieira,

H. S. MacIel, *Vacuum* **2016**, *123*, 91.

[26] H. Tang, R. Sanjinès, P. E. Schmid, F. Lévy, *J. Appl. Phys.* **1994**, *75*, 2042.

[27] M. Ritala, M. Leskelä, E. Nykanen, P. Soininen, L. Niinisto, *Thm Solid Film.* **1993**, *225*, 288.

[28] S. K. Cheung, N. W. Cheung, *Appl. Phys. Lett.* **1986**, *49*, 85.

[29] G. Güler, Ö. Güllü, Ş. Karataş, Ö. F. Bakkalolu, *J. Phys. Conf. Ser.* **2009**, *153*.

[30] Z. Zhang, J. T. Yates, *Chem. Rev.* **2012**, *112*, 5520.

[31] I. Marri, S. Ossicini, *Solid State Commun.* **2008**, *147*, 205.

[32] T. Liu, M. Dupuis, C. Li, *J. Phys. Chem. C* **2016**, *120*, 6930.

[33] Y. Yin, A. Sibley, J. S. Quinton, D. A. Lewis, G. G. Andersson, *Adv. Funct. Mater.* **2018**, *28*, 1.

[34] J. Meyer, *J. Photonics Energy* **2011**, *1*, 011109.

[35] M. T. Greiner, M. G. Helander, W. M. Tang, Z. Bin Wang, J. Qiu, Z. H. Lu, *Nat. Mater.* **2012**, *11*, 76.

[36] Irfan, M. Zhang, H. Ding, C. W. Tang, Y. Gao, *Org. Electron.* **2011**, *12*, 1588.

[37] Y. Yin, X. Pan, M. R. Andersson, D. A. Lewis, G. G. Andersson, *ACS Appl. Energy Mater.* **2020**, *3*, 366.

[38] J. Meyer, S. Hamwi, M. Kröger, W. Kowalsky, T. Riedl, A. Kahn, *Adv. Mater.* **2012**, *24*, 5408.

[39] Y. Zhang, O. Pluchery, L. Caillard, A. F. Lamic-Humblot, S. Casale, Y. J. Chabal, M. Salmeron, *Nano Lett.* **2015**, *15*, 51.

[40] L. V. Besteiro, X. T. Kong, Z. Wang, G. Hartland, A. O. Govorov, *ACS Photonics* **2017**, *4*, 2759.

[41] F. M. Spirkl, S. Kunz, F. F. Schweinberger, A. N. Farnbacher, R. Schröter, U. Heiz, *Rev. Sci. Instrum.* **2012**, *83*.

[42] K. Volgmann, F. Voigts, W. Maus-Friedrichs, *Surf. Sci.* **2012**, *606*, 858.

[43] S. Park, J. Jeong, G. Hyun, M. Kim, H. Lee, Y. Yi, *Sci. Rep.* **2016**, *6*, 1.

[44] G. Krishnan, H. S. Al Qahtani, J. Li, Y. Yin, N. Eom, V. B. Golovko, G. F. Metha, G. G. Andersson, *J. Phys. Chem. C* **2017**, *121*, 28007.

[45] G. Krishnan, N. Eom, R. M. Kirk, V. B. Golovko, G. F. Metha, G. G. Andersson, *J. Phys. Chem. C* **2019**, *123*, 6642.